

Self-propulsion mechanism of active Janus particles in near-critical binary mixtures

Sela Samin* and René van Roij

*Institute for Theoretical Physics, Center for Extreme Matter and Emergent Phenomena,
Utrecht University, Leuvenlaan 4, 3584 CE Utrecht, The Netherlands*

(Dated: March 2, 2024)

Gold-capped Janus particles immersed in a near-critical binary mixture can be propelled using illumination. We employ a non-isothermal diffuse interface approach to investigate the self-propulsion mechanism of a single colloid. We attribute the motion to body forces at the edges of a micron-sized droplet that nucleates around the particle. Thus, the often-used concept of a surface velocity cannot account for the self-propulsion. The particle's swimming velocity is related to the droplet shape and size, which is determined by a so-called critical isotherm. Two distinct swimming regimes exist, depending on whether the droplet partially or completely covers the particle. Interestingly, the dependence of the swimming velocity on temperature is non-monotonic in both regimes.

The study of self-propelling synthetic colloids is an area of intense active research [1, 2]. The out-of-equilibrium directed motion of these colloidal microswimmers is maintained by a constant energy input which originates from their own activity. The directed swimming, coupled to the particle's rotational diffusion, leads to a significant increase in the effective diffusion coefficient [3–5] and to complex collective behavior, such as dynamical phase-separation [6–8] and clustering [9–11]. Optimization of the microswimmers design is essential for realizing applications such as targeted cargo and drug delivery, parallel assembly and scavenging of contaminants [1, 12, 13].

The design of synthetic swimmers requires an understanding of the underlying mechanisms for the self-propulsion, *e.g.* self-diffusiophoresis [3, 14–18], self-induced electrophoretic flow, [19, 20] and self-thermophoresis [4, 21]. In many realizations, the particle motion is attributed to a microscopically thin boundary layer adjacent to the solid-fluid interface, which interacts with a self-generated field, such as electrical potential, solute concentration and temperature. Body forces within this layer give rise to an apparent slip velocity at the surface [22] while the fluid outside the interfacial layer is considered force-free. Thus, the particle motion is completely determined by the slip velocity distribution on its surface [17, 23]. However, this simple picture breaks down when the self-generated field extends to a region with a size similar to that of the particle. In this Letter we explore such a scenario of self-diffusiophoresis due to a local solvent demixing, leading to a complex swimming behavior arising from the coupling of the self-generated chemical potential gradients and the fluid motion.

We focus on a recently realized new class of swimmer consisting of Janus colloids immersed in a near-critical binary mixture. Local heating of the colloid surface and the ensuing solvent demixing propels these particles, which exhibit fascinating individual and collective behaviour [5, 6, 24–26]. A similar system was studied by Araki and Fukai [27] but in their simulations heating is periodically applied to the whole mixture. In this work we study the self-propulsion mechanism of a locally heated

Janus swimmer (illustrated in Fig. 1) and show that it is fundamentally different from motion driven by interfacial velocities. Rather, we find that the particle motion is linked to the flow at the edges of a stationary demixed droplet, also far from the particle surface, and that it depends strongly on the solvent and particle properties. These advective effects are ignored in Würger's recent study of a similar system [28].

We consider a micron-sized spherical colloid with radius R immersed in an unbounded homogeneous near-critical binary mixture. Half of the particle is gold-capped and continuously heated by irradiation. The gold layer thickness is typically of the order of 10nm, much smaller than the colloid radius, and its thermal conductivity is much larger than that of the liquid and colloid. Thus, the cap forms an isotherm [21] with a temperature $T_0 > T_\infty$, where T_∞ is the fluid's ambient temperature far from the colloid. Local demixing of the fluid occurs if the temperature around the colloid increases above the (lower) critical temperature T_c of the mixture, of which both components are assumed to have a molecular volume a^3 with $a \sim 3\text{\AA}$. Consequently, temperature gradients in the demixed phase lead to gradients of the mixture chemical potential which give rise to a local body-force. From azimuthal symmetry, no net torque will act on the colloid but since the temperature field is not spherically symmetric, the demixed droplet exerts a net force on the

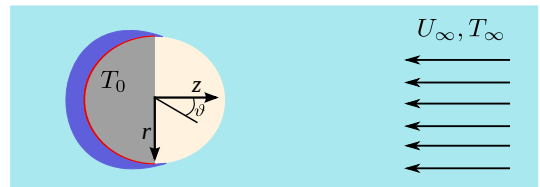


FIG. 1. Schematic illustration of a Janus particle immersed in a near-critical binary mixture at a temperature $T_\infty < T_c$. Illumination results in $T_0 > T_c$ at the gold-capped hemisphere (red line). At steady state, a demixed droplet is nucleated around the translating colloid, with a fluid velocity U_∞ at infinity in the frame-of-reference co-moving with the particle.

colloid in the axial direction. Hence, we set a cylindrical coordinate system in a frame-of-reference co-moving with a colloid placed at its origin. Our aim is to find the axial velocity of the fluid far away from the colloid: $U_\infty = -U_\infty \hat{z}$ such that the colloid is force-free. The main result of this paper is that the self-propulsion is a result of forces perpendicular to the colloid surface, and cannot be attributed to an effective surface velocity parallel to it, as is common in many scenarios [14, 17, 21, 22].

We investigate the steady-state during the ballistic motion of the colloid at a time scale much shorter than its rotational diffusion time [24]. To this end we employ a well-established diffuse interface based approach [29], that couples the mixture order parameter $\varphi \in [-1/2, 1/2]$, the mixture chemical potential $k_B T \mu$, the fluid velocity $U_\infty \mathbf{v}$, and the scaled temperature $\Theta = (T - T_\infty)/(T_0 - T_\infty)$ by the dimensionless equations:

$$\partial\varphi/\partial t = -\nabla \cdot (\text{Pe}_\varphi \varphi \mathbf{v} - \nabla\mu) , \quad (1)$$

$$\mu = -\epsilon \nabla^2 \varphi + f'(\varphi) , \quad (2)$$

$$\nabla \cdot \mathbf{v} = 0 , \quad (3)$$

$$\nabla \cdot \boldsymbol{\tau} = \nabla p + \text{C}_h^{-1} \text{Ca}^{-1} \varphi \nabla \mu , \quad (4)$$

$$\text{Le}^{-1} \partial\Theta/\partial t = -\nabla \cdot (\text{Pe}_T \Theta \mathbf{v} - \nabla\Theta) . \quad (5)$$

Here, all lengths are scaled by R and time is scaled by R^2/D , where D is the mixture inter-diffusion constant.

Eq. (1) is the convective Cahn-Hilliard equation governing the composition dynamics, where the relative magnitude of the composition advective flux, $\varphi \mathbf{v}$, and diffusive flux, $D \nabla \mu$, is measured by the composition Péclet number, $\text{Pe}_\varphi = U_\infty R/D$. The chemical potential Eq. (2) is obtained via the bulk free energy $a^3 f = (\chi - 2)\varphi^2 + 4\varphi^4/3$, where $\chi \sim 1/T$ is the Flory interaction parameter, supplemented by the square-gradient term which accounts for interfacial tension [30]. The interfacial width is characterized by $\epsilon = \chi \text{C}_h^{-2}$, where $\text{C}_h = a/R$ is the Cahn number. Eqs. (3) and (4) are the Stokes equations governing the fluid flow. Here, p and $\boldsymbol{\tau} = \nabla \mathbf{v} + \nabla \mathbf{v}^T$ are the dimensionless fluid pressure and viscous stress tensor, respectively, scaled by $\eta_f U_\infty / R$, where η_f is the fluid viscosity. The last term in Eq. (4) is the body force due to gradients in the chemical potential, it is proportional to the inverse capillary number, $\text{Ca} = a^2 \eta_f U_\infty / k_B T$, which measures the relative magnitude of viscous and surface tension forces. Eq. (5) is the energy equation for the fluid. Here, $\text{Pe}_T = U_\infty R/\alpha$ is the thermal Péclet number, where $\alpha_f = k_f/(\rho_f C_f)$ is the fluid thermal diffusivity, and ρ_f , C_f and k_f are the fluid density, heat capacity and thermal conductivity, respectively. The Lewis number, $\text{Le} = \alpha_f/D$, is the ratio of thermal to mass diffusivity.

The force, \mathbf{F} , exerted on the colloid by the fluid is estimated by applying the divergence theorem to Eq. (4):

$$\mathbf{F} = 2\pi \int_{-1}^1 dc \, c [p \mathbb{1} + \Pi - \boldsymbol{\tau}] \cdot \mathbf{n} , \quad (6)$$

where $c = \cos \vartheta$, ϑ is the polar angle and \mathbf{n} is the outward unit vector normal to the surface. By recasting $\varphi \nabla \mu = \nabla \cdot \Pi$ one obtains [29] the Korteweg stress tensor, $\Pi = [\varphi f'(\varphi) - f - \frac{1}{2} \epsilon |\nabla \varphi|^2 - \epsilon \varphi \nabla^2 \varphi] \mathbb{1} + \epsilon \nabla \varphi \nabla \varphi$.

The physical properties are taken to best mimic the experimental setup in Ref. [24]. Therefore, we use properties of silica glass for the colloid and those of a critical water-2,6-lutidine for the fluid. Since $T_0 - T_\infty$ is only of the order of 1K we can assume that all material properties are constant [30], see the caption of Fig. 2 for the values used in the calculation. The assumption that D is constant is a somewhat crude approximation, since it vanishes as a power law close to T_c [31]. In the temperature window we examine D is of the order of $10^{-11} - 10^{-12} \text{m}^2/\text{s}$ [32]. We therefore use an ‘‘effective’’ value of D as a parameter and examine its influence on the swimming. In addition, the exact value of the contact angle of each hemisphere in water-2,6-lutidine is unknown. We therefore use an indicative contact angle of $\theta_1 = \pi/4$ for the hydrophilic gold cap throughout this work such that $\varphi > 0$ corresponds to a water-rich phase. We will explore the influence of θ_2 at the other hemisphere on the swimming.

Taking $R = 0.5 \mu\text{m}$, $D = 4 \times 10^{-11} \text{m}^2/\text{s}$ and a large $U_\infty = 20 \mu\text{m}/\text{s}$ leads to $\text{Pe}_\varphi \approx 0.2$, $\text{Pe}_T \approx 10^{-4}$, $\text{Le} \approx 10^3$, $\text{C}_h \approx 10^{-4}$ and $\text{Ca} \approx 10^{-5}$. Even for this extremal U_∞ , $\text{Pe}_T \ll 1$ and we can safely neglect the heat advection in Eq. (5). In addition, because heat diffuses much faster than mass, $\text{Le} \gg 1$, the temperature adjusts almost instantly to a composition perturbation and we may neglect also the time dependence in Eq. (5), which leads to the heat equation $\nabla^2 \Theta = 0$. The same argument holds for the solid where we also solve the Laplace equation. Hence, the temperature distribution *only* depends on the thermal conductivity contrast of the solid and fluid, k_s/k_f , where k_s is the colloid thermal conductivity. Therefore, we solve the heat equation once, and use the resulting temperature distribution as an input for the relaxation of the velocity and composition. This relaxation is dominated by the body force $\varphi \nabla \mu$ in Eq. (4) since $\text{Ca} \ll 1$.

The colloid is placed at the origin of a large cylindrical domain of height $z \in [-L, L]$ and radius $r \in [0, L]$ with $L = 500$ [30]. We use symmetry boundary conditions (BCs) at $r = 0$. At the other edges of the domain we impose, using the appropriate BCs, a mixture of critical composition at a temperature T_∞ ($\Theta = 0$) with a velocity U_∞ [30]. On both colloid hemispheres we impose a no-slip BC for the fluid: $\mathbf{v}_i = 0$, where $i = 1, 2$ denotes the capped and uncapped hemisphere, respectively. At the capped hemisphere we set $\Theta_1 = 1$ while for the uncapped hemisphere we have continuity of the heat flux, $\mathbf{n} \cdot k_f \nabla \Theta_{out} = \mathbf{n} \cdot k_s \nabla \Theta_{in}$. The first BC for the composition at the colloid surface is no flux: $\mathbf{n} \cdot \nabla \mu = 0$. The colloid has two chemically distinct solid-liquid interfaces, for which we assume an excess surface

free energy F_w of the form $a^2 F_w/k_B T = \sum_i \int \gamma_i \varphi dA_i$, where γ_i measures the difference between the microscopic short-range interaction of the two solvent components and the solid. The wetting angles θ_i are then imposed using: $\mathbf{n} \cdot \nabla \varphi = -\tan(\pi/2 - \theta_i) |(1 - \mathbf{n}\mathbf{n}) \cdot \nabla \varphi|$, where in this so-called geometric formulation of the wetting BC $\gamma_i = \cos \theta_i / \sqrt{2}$ [33]. This BC has proved useful in simulations of moving contact lines where it is known to result in an effective slip through the diffusive fluxes between the phases [33–35]. Thus, fluid motion due to the interaction with the surface is actually resolved even though the no-slip BC is imposed.

Modern day computational resources coupled to specialized mesh generation allowed us to resolve the fluid spatial distribution over 6 orders of magnitude, from the microscopic scale set by the interfacial width, $O(a)$, up to the mesoscopic scale set by the domain size L [30].

Steady State. The resulting composition of the mixture around a force-free swimmer ($\mathbf{F} = 0$) for several T_∞ and fixed $T_0 = T_c + 0.5\text{K}$ is shown in Fig. 2 (a)-(d). The solid red line in each panel is the contour of the reduced critical temperature, $\Theta_c = (T_c - T_\infty)/(T_0 - T_\infty)$, which can account for many features of the swimming. Demixing only occurs inside the region bounded by the Θ_c isotherm, where $T > T_c$. In Fig. 2 (a) we also show several other contours of $\Theta < \Theta_c$ (dashed lines). Demixing within these contours will occur for fixed $T_0 > T_c$ and increasing T_∞ [see Fig. 2 (b)-(d)] or for fixed T_∞ and increasing T_0 . In both cases Θ_c decreases and thus the droplet grows.

Fig. 2 also reveals that a single water-rich droplet is nucleated at the particle surface. Within the droplet the composition is inhomogeneous; φ is maximal at the surface and decays rather smoothly to the bulk value $\varphi = 0$ because of the temperature gradients and the proximity to T_c . The demixed region is clearly distinct from the bulk phase, as can be seen from the velocity vectors. Inside the demixed region the velocity is very small implying the droplet effectively moves together with the particle. Strikingly, we find that *no* significant slip occurs at the surface, in contrast to the results in Ref. [28]. The fluid weakly circulates inside the droplet [30] and the overall flow pattern is similar to that of Stokes flow past a viscous droplet [36].

We distinguish between two droplet shapes: (i) when $\Theta_c < \Theta_{\text{cov}}$ the droplet partially covers the particle as in Fig. 2 (a)-(c) and (ii) for $\Theta_c > \Theta_{\text{cov}}$ complete covering occurs as in Fig. 2 (d). The covering temperature Θ_{cov} is closely related to the uncapped pole isotherm $\Theta_p = \Theta_c$, for which the demixed region should first encompass the particle. For the solid-fluid heat conductivity contrast $k_s/k_f \approx 3.5$ that we use, $\Theta_p \approx 0.7$. However, a thin demixed region at the pole is energetically costly, and in fact our numerical solution gives $\Theta_{\text{cov}} \approx 0.66$ somewhat smaller than Θ_p and a discontinuity in the pole composition at Θ_{cov} . In comparison, for $k_s/k_f = 1$ the lower heat diffusivity in the solid leads to $\Theta_p = 0.5$ [21]. Hence, the

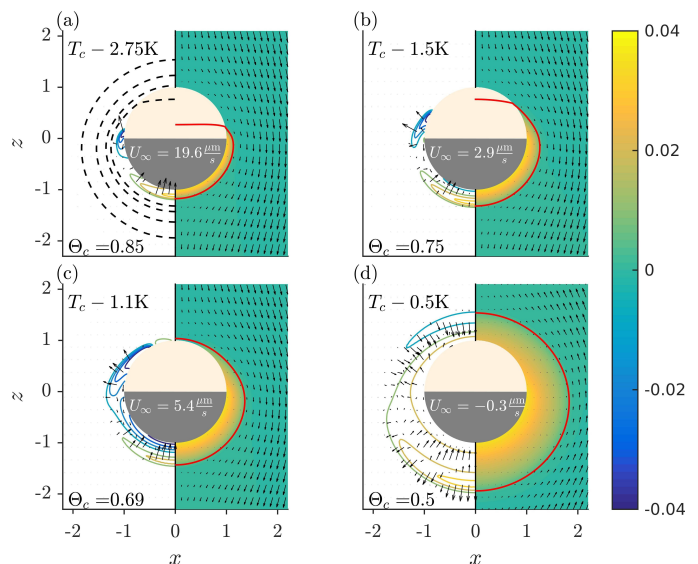


FIG. 2. Steady state composition φ (right) and contours of the scaled pressure $p/200$ (left) around a heated Janus particle in the xOz plane. The temperature of the heated cap is $T_0 = T_c + 0.5\text{K}$. The bulk mixture temperature approaches T_c from (a) to (d) with $T_c - T_\infty$ equal to (a) 2.75K, (b) 1.5K, (c) 1.1K and (d) 0.5K. The red curve is the critical contour Θ_c . Arrows are vectors of the velocity (right) and body force [Eq. (4)] (left). In (a) the dashed lines are the contours $\Theta = 0.75, 0.69, 0.6, 0.5$. Here, $D = 4 \times 10^{-11} \text{ m}^2/\text{s}$, $\theta_1 = \pi/4$ and $\theta_2 = \pi/2$. For the physical properties of the 2,6-lutidine-water mixture we take $a = 3.4\text{\AA}$, $\rho_f = 987 \text{ kg/m}^3$, $\eta_f = 2 \text{ mPa s}$, $C_f = 4.3 \text{ kJ}/(\text{kg K})$ and $k_f = 0.39 \text{ W}/(\text{m K})$ [37–39]. For the silica particle we used $k_s = 1.38 \text{ W}/(\text{m K})$.

droplet shape and therefore the swimming behavior are both quite sensitive to the conductivity contrast, which we thus identify as an interesting engineering parameter.

To maintain the steady-state shape of the droplet as dictated by the contour Θ_c , the composition diffusive flux $\propto \nabla \mu$ balances the convective flux according to Eq. (1). Therefore, the body force $\propto \varphi \nabla \mu$ is primarily large at the droplet diffuse boundary where advection becomes significant, see the vector maps in Fig. 2 (a)-(c). The body force may be large within the droplet when U_∞ is small and the droplet internal dynamics also becomes significant, see Fig. 2 (d). Notice that the pressure contours in Fig. 2 are approximately perpendicular to $\varphi \nabla \mu$ because within the droplet $\nabla \cdot \tau$ is small, and thus $\nabla p \propto \varphi \nabla \mu$ to first-order at steady-state. Moreover, at the front of the droplet (with respect to the particle direction of motion) the diffusive flux must balance an advective flux toward the droplet whereas at the rear of the droplet the advective flux carries the mixture away from the droplet. Thus, also the body force at the droplet edge acts in opposite directions relative to the fluid flow, resulting in the pressure distributions of Fig. 2 (a)-(c) exhibiting two regions: (i) a $p > 0$ region at the droplet rear and (ii) a region of $p < 0$ near the three phase contact line.

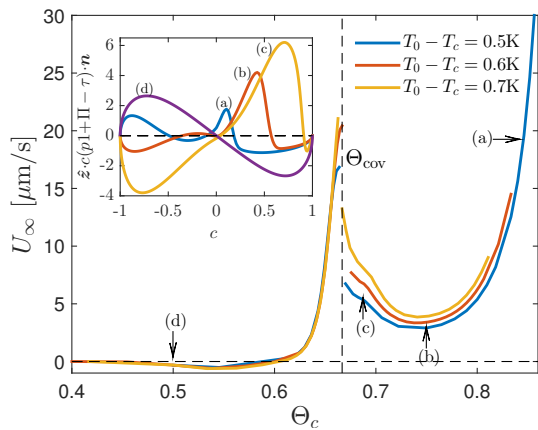


FIG. 3. Swimming velocity vs. reduced critical temperature curves for three quenching temperatures $T_0 - T_c$. The droplet completely covers the colloid for $\Theta_c < \Theta_{cov} \approx 0.66$ whereby the different curves collapse onto one another. For $\Theta_c > \Theta_{cov}$ the curves are distinct with the swimming velocity increasing with quenching. The velocity of the swimmers in Fig. 2 in indicated with arrows and the inset shows the corresponding force profiles along the colloid contour.

The anisotropy of the droplet shape produces an anisotropy also of the pressure and body force within the droplet, which is responsible for the particle motion. Thus, the self-propulsion is a result of forces perpendicular to the surface, which are affected by the flow far from the surface, and cannot be mapped to an effective surface velocity. In Fig. 2 (a)-(c), the resulting force-free motion is in the direction of the uncapped hemisphere whereas the completely covered colloid in Fig. 2 (d) moves with the capped hemisphere on the front.

Swimming Velocity. Fig. 3 shows the swimming velocity U_∞ as a function of Θ_c for three values of the quenching $T_0 - T_c$, which increases with the laser intensity in experiments. U_∞ strongly depends on Θ_c and is of the order of $0.1 - 10 \mu\text{m/s}$, in agreement with experiments. Two swimming regimes exist, for complete coverage at $\Theta_c < \Theta_{cov}$ the swimming is independent of the quenching as Θ_c completely determines the demixed state. In contrast, for $\Theta_c > \Theta_{cov}$ the curves are distinct with U_∞ increasing with quenching. This is because here Θ_c meets the particle surface at an angle different from the contact angle, which leads to a competition between the demixing and surface energies close to the three phase contact line, with the balance shifted in favor of the demixing as quenching increases. Experiments are performed at a single constant T_∞ , showing that the swimming velocity increases with the laser intensity [24], but our calculations, which explore a large range of T_∞ , indicate this is not always the case.

Fig. 3 also reveals that U_∞ jumps at Θ_{cov} and is non-monotonic with Θ_c in both regimes. To understand this behaviour we plot in the inset of Fig. 3 the z component of the force [cf. Eq. (6)] along the particle contour,

$\hat{z} \cdot c(p\mathbf{1} + \Pi - \tau) \cdot \mathbf{n}$, as function of c , where $c < 0$ ($c > 0$) corresponds the (un)capped hemisphere. The labels in the inset and the arrow labels in Fig. 3 correspond to the swimmers in the panels of Fig. 2. When Θ_c and U_∞ are large, as in Fig. 2 (a), the force profile has a positive maximum in each hemisphere. This is because the droplet is small and hence a large body force exists close to the surface at both hemispheres. When Θ_c decreases and the droplet grows, as in Fig. 2 (b)-(c), the positive maximum at the capped hemisphere becomes a negative minimum while the maximum at the uncapped hemisphere grows in magnitude and moves to a larger c . This is a result of the anisotropic shape of the droplet. While the Θ_c contour is distanced from the capped hemisphere it remains close to the uncapped hemisphere and also covers a larger portion of it. Thus, the body force localized at the droplet edge becomes more significant near the three phase contact line rather than near the particle rear, thereby accounting for the minimum in U_∞ . For $\Theta_c < \Theta_{cov}$, U_∞ first jumps to a larger positive value but decreases with Θ_c and eventually becomes negative, since now the droplet edge at the front is also distanced from the particle. Finally, U_∞ vanishes when Θ_c is small and the large droplet becomes quasi-spherical ($T_\infty \rightarrow T_c$).

The nucleation of a second, water-poor droplet, at the uncapped hemisphere is unfavored unless the hemisphere is very hydrophobic. The small volume of the demixed region around the uncapped hemisphere compared to the capped counterpart entails a relatively larger surface energy penalty. Nonetheless, we find that for $\theta_2 \gtrsim 0.8\pi$ a water-poor droplet does nucleate at the uncapped hemisphere. This is accompanied by a reversal of the swimming direction [30]. Assuming that the uncapped silica is hydrophilic [24, 40], this result is consistent with the experimental observation that particles with a hydrophilic gold cap swim with their cap at the rear whereas for a hydrophobic cap it is at the front [24].

We also examined the dependence of U_∞ on the diffusion constant. For a swimmer with the same parameters as in Fig. 2 (b) but with D 10-fold larger or smaller, the resulting velocity is $111 \mu\text{m/s}$ and $0.36 \mu\text{m/s}$, respectively. As expected, U_∞ increases with D because the diffusive current is able to compensate for larger advection while maintaining the droplet shape. Further work is required to understand the more realistic scenario where D may vary in space due to thermal gradients near T_c .

In conclusion, we have shown that a locally heated Janus particle in a near-critical binary mixture is propelled by the chemical potential gradients at the diffuse interface of a nucleated droplet, arising from the balance of diffusive and advective fluxes. Therefore, the self-propulsion cannot be described by an effective surface velocity. We hope that our results will stimulate further experiments to uncover the details of the swimming mechanisms of these intriguing particles and possibly explore other microswimmers propelled by non-local

self-generated fields.

We acknowledge fruitful discussions with C. Bechinger and J. de Graaf and financial support of a Netherlands Organisation for Scientific Research (NWO) VICI grant funded by the Dutch Ministry of Education, Culture and Science (OCW). This work is part of the D-ITP consortium, a program of the Netherlands Organisation for Scientific Research (NWO) funded by the Dutch Ministry of Education, Culture and Science (OCW).

* S.Samin@uu.nl

- [1] S. J. Ebbens and J. R. Howse, *Soft Matter* **6**, 726 (2010).
- [2] I. S. Aranson, *Physics-Usppekhi* **56**, 7992 (2013).
- [3] J. R. Howse, R. A. L. Jones, A. J. Ryan, T. Gough, R. Vafabakhsh, and R. Golestanian, *Phys. Rev. Lett.* **99**, 048102 (2007).
- [4] H.-R. Jiang, N. Yoshinaga, and M. Sano, *Phys. Rev. Lett.* **105**, 268302 (2010).
- [5] G. Volpe, I. Buttinoni, D. Vogt, H.-J. Kummerer, and C. Bechinger, *Soft Matter* **7**, 8810 (2011).
- [6] I. Buttinoni, J. Bialké, F. Kümmel, H. Löwen, C. Bechinger, and T. Speck, *Phys. Rev. Lett.* **110**, 238301 (2013).
- [7] J. Stenhammar, A. Tiribocchi, R. J. Allen, D. Marenduzzo, and M. E. Cates, *Phys. Rev. Lett.* **111**, 145702 (2013).
- [8] T. Speck, J. Bialké, A. M. Menzel, and H. Löwen, *Phys. Rev. Lett.* **112**, 218304 (2014).
- [9] I. Theurkauff, C. Cottin-Bizonne, J. Palacci, C. Ybert, and L. Bocquet, *Phys. Rev. Lett.* **108**, 268303 (2012).
- [10] J. Palacci, S. Sacanna, A. P. Steinberg, D. J. Pine, and P. M. Chaikin, *Science* **339**, 936940 (2013).
- [11] O. Pohl and H. Stark, *Phys. Rev. Lett.* **112**, 238303 (2014).
- [12] M. N. Popescu, M. Tasinkevych, and S. Dietrich, *EPL* **95**, 28004 (2011).
- [13] L. Baraban, M. Tasinkevych, M. N. Popescu, S. Sanchez, S. Dietrich, and O. G. Schmidt, *Soft Matter* **8**, 4852 (2012).
- [14] R. Kapral, *J. Chem. Phys.* **138**, 020901 (2013).
- [15] R. Golestanian, T. B. Liverpool, and A. Ajdari, *Phys. Rev. Lett.* **94**, 220801 (2005).
- [16] U. M. Córdova-Figueroa and J. F. Brady, *Phys. Rev. Lett.* **100**, 158303 (2008).
- [17] J. F. BRADY, *J. Fluid Mech.* **667**, 216259 (2010).
- [18] J. de Graaf, G. Rempfer, and C. Holm, *IEEE Transactions on NanoBioscience* **14**, 272288 (2015).
- [19] W. F. Paxton, K. C. Kistler, C. C. Olmeda, A. Sen, S. K. St. Angelo, Y. Cao, T. E. Mallouk, P. E. Lammert, and V. H. Crespi, *J. Am. Chem. Soc.* **126**, 1342413431 (2004).
- [20] J. L. MORAN and J. D. POSNER, *J. Fluid Mech.* **680**, 3166 (2011).
- [21] T. Bickel, A. Majee, and A. Würger, *Phys. Rev. E* **88**, 012301 (2013).
- [22] J. L. Anderson, *Annu. Rev. Fluid Mech.* **21**, 6199 (1989).
- [23] T. Bickel, G. Zecua, and A. Würger, *Phys. Rev. E* **89**, 050303 (2014).
- [24] I. Buttinoni, G. Volpe, F. Kümmel, G. Volpe, and C. Bechinger, *J. Phys.: Condens. Matter* **24**, 284129 (2012).
- [25] B. ten Hagen, F. Kümmel, R. Wittkowski, D. Takagi, H. Löwen, and C. Bechinger, *Nat Commun* **5**, 4829 (2014).
- [26] F. Kümmel, B. ten Hagen, R. Wittkowski, I. Buttinoni, R. Eichhorn, G. Volpe, H. Löwen, and C. Bechinger, *Phys. Rev. Lett.* **110**, 198302 (2013).
- [27] T. Araki and S. Fukai, *Soft Matter* **11**, 3470 (2015).
- [28] A. Würger, *ArXiv e-prints* (2015), arXiv:1504.01522 [cond-mat.soft].
- [29] D. M. Anderson, G. B. McFadden, and A. A. Wheeler, *Annu. Rev. Fluid Mech.* **30**, 139165 (1998).
- [30] For details see the supplementary material.
- [31] K. Kawasaki, *Annals of Physics* **61**, 1 (1970), cited By 384.
- [32] E. Güllari, A. F. Collings, R. L. Schmidt, and C. J. Pings, *J. Chem. Phys.* **56**, 6169 (1972).
- [33] H. Ding and P. D. M. Spelt, *Phys. Rev. E* **75**, 046708 (2007).
- [34] H.-Y. Chen, D. Jasnow, and J. Viñals, *Phys. Rev. Lett.* **85**, 1686 (2000).
- [35] D. JACQMIN, *J. Fluid Mech.* **402**, 5788 (2000).
- [36] C. Pozrikidis, *Introduction to Theoretical and Computational Fluid Dynamics* (Oxford University Press, USA, 2011).
- [37] C. A. Grattoni, R. A. Dawe, C. Y. Seah, and J. D. Gray, *J. Chem. Eng. Data* **38**, 516 (1993).
- [38] S. Pittois, G. P. Sinha, C. Glorieux, and J. Thoen, in *Thermal Conductivity 27/Thermal Expansion 15*, edited by H. Wang and W. Porter (DEStech Publications, 2004).
- [39] S. Z. Mirzaev, R. Behrends, T. Heimbürg, J. Haller, and U. Kaatz, *J. Chem. Phys.* **124**, 144517 (2006).
- [40] P. D. Gallagher and J. V. Maher, *Phys. Rev. A* **46**, 2012 (1992).